RSC Advances

PAPER

Cite this: *RSC Adv.*, 2015, **5**, 108058

Block-shaped pure and doped $Li_4Ti_5O_{12}$ containing a high content of a Li_2TiO_3 dual phase: an anode with excellent cycle life for high rate performance lithium-ion batteries

Emad M. Masoud*[a] and Sylvio Indris[b]

Received 29th October 2015
Accepted 27th November 2015

DOI: 10.1039/c5ra22745c

www.rsc.org/advances

Pure and doped lithium titanate samples ($Li_4Ti_5O_{12}$, $Li_4Ti_{4.9}x_{0.1}O_{12}$, x = Ni^{2+}, Cu^{2+} and Zn^{2+}) are prepared using a simple solid state reaction. All lithium titanate samples are characterized using X-ray diffraction, Fourier transform infrared spectroscopy and scanning electron microscopy. X-ray diffraction patterns show a cubic spinel structure of $Li_4Ti_5O_{12}$ with different contents of a Li_2TiO_3 crystalline second phase, high for the doped samples and low for the pure one. Fourier transform infrared spectra also confirm the spinel structure. Scanning electron microscopy shows block-shaped particles with different particle size distributions. The pure lithium titanate composite sample shows more efficient electrochemical performance than the doped ones at high discharge rates (2–30C) and the opposite is observed at low ones (0.1, 0.5C). The efficiency and cycle life of the pure lithium titanate composite at a high rate (30C) are higher and better than that at a low one (0.1C), making the pure composite a promising anode material for high rate lithium-ion batteries. All results are collected and discussed.

1. Introduction

Stimulated by the urgency of environmental protection and the exhaustion of fossil fuel reserves, more and more attention has been paid to the development of lithium ion batteries with high power density for the applications of large format energy storage systems, such as electric vehicles (EVs) or hybrid electrical vehicles (HEVs).[1] At present, one of the main factors that hinders the commercialization of EVs/HEVs is the low rate performance of batteries. Therefore, an urgent step for the significant market penetration of EVs/HEVs is the development of a high rate battery system. The anode is one of the most important parts of a battery. Considering carbon based anodes, the low operating potential of 100 mV (*vs.* Li^+/Li) tends to induce the growth of lithium dendrites at high charge/discharge rates, which make a short circuit possible.[2] Alternative anode materials of silicon and tin have been extensively studied for their attractive specific capacities.[3] However, the poor cycle stability caused by immense volume expansion in the process of lithiation stands in the way of commercialization. In spite of the less competitive specific energy density relative to carbon, tin, and silicon-based materials, spinel lithium titanate ($Li_4Ti_5O_{12}$) is considered as one of the most promising anodes for its higher discharge/charge plateau (about 1.55 V *vs.* Li^+/Li) and zero strain characteristic which can provide possible solutions to the challenges of safety and cycle stability for advanced batteries.[4–6] Evidently, it is the poor rate performance resulting from quite low electronic conductivity (<10^{-13} S cm^{-1})[7] and intermediate Li ion conductivity of pristine $Li_4Ti_5O_{12}$ that retards it from commercialization.

Traditional methods for improving electronic conductivity and ionic conductivity mainly focus on cation doping (Mg, Al, V, *etc.*[7–11]), surface modification (carbon, polyacene, *etc.*[12–17]) and size control.[18,19] More recently, composites of $Li_4Ti_5O_{12}$/Ag,[20–23] $Li_4Ti_5O_{12}$/Au,[24] $Li_4Ti_5O_{12}$/Cu,[25,26] and $Li_4Ti_5O_{12}$/CNT[27] have been widely investigated to improve particle-to-particle and particle-to-current collector electrical contact. Alternatively, nano composites of $Li_4Ti_5O_{12}$ and metal oxides can provide rich grain boundaries with a high concentration of diffusion-mediating defects, which make fast diffusivity possible. In this regard, dual-phase $Li_4Ti_5O_{12}$–TiO_2 has been synthesized with improved rate capability.[28–30] According to the literature, there is one report considering the impact of Li_2TiO_3 second phase traces on the electrochemical performance of $Li_4Ti_5O_{12}$.[31] Here, we want to study the effect of doping with Zn^{2+}, Cu^{2+} and Ni^{2+} on the electrochemical performance of $Li_4Ti_5O_{12}$ in the presence of a high content crystalline second phase of Li_2TiO_3 at low and high rates comparing to the undoped material, to show which can deliver a high capacity and good cycle life at high rates.

[a]*Chemistry Department, Faculty of Science, Benha University, 13518 Benha, Egypt. E-mail: emad.youssef@fsc.bu.edu.eg; emad_masoud1981@yahoo.com; Tel: +20 1203532343*

[b]*Karlsruhe Institute of Technology, Institute for Applied Materials (IAM), Hermann-von-Helmholtz-Platz 1, D-76344 Eggenstein-Leopoldshafen, Germany*

2. Experimental

2.1 Preparation of samples

All samples were prepared using a solid-state reaction method. Li_2CO_3 (Merck, 99.99%), TiO_2 (Sigma-Aldrich, 99.9%), NiO (Sigma-Aldrich, 99.99%), CuO (Sigma-Aldrich, 99.99%) and ZnO (Sigma-Aldrich, 99.99%) powders were used to prepare the pure and doped lithium titanate samples ($Li_4Ti_5O_{12}$, $Li_4Ti_{4.9}x_{0.1}O_{12}$, $x = Ni^{2+}$, Cu^{2+} and Zn^{2+}). A 4 : 5 molar ratio of Li_2CO_3 : TiO_2 for the pure sample and a 4 : 4.9 : 0.1 molar ratio of Li_2CO_3 : TiO_2 : dopant source for the doped samples were firstly ball-milled in the presence of ethanol as a dispersion medium for 3 h in a ball-milling machine to homogeneously mix the powders. In all cases, 3 mol% excessive Li_2CO_3 was added to compensate for Li_2O evaporation during the synthesis at high temperature. All samples were dried at 90 °C for 30 minutes to remove the ethanol, and then the milled mixtures were calcined at 800 °C for 4 h in air.

2.2 Characterization of samples

X-ray diffraction (XRD) analysis was performed on a STOE STADI P diffractometer (Cu-Kα radiation, Germanium monochromator, Debye–Scherrer geometry). The samples were measured at room temperature in the range from $2\theta = 10°$ to 70°. The XRD phases present in the samples were identified with the help of ASTM powder data files. The infrared spectra of samples were recorded in the range of 400–4000 cm^{-1} using a Bruker-FTIR. The morphology of the samples were examined using scanning electron microscopy (SEM, JEOL JSM-6700F) operated at an accelerating voltage of 5 kV.

The electrical measurements were carried out in the form of a pellet. The two parallel surfaces of the pellet were coated with silver paste to ensure good electrical contact. The sample was placed in a sample holder inside a cryostat with a temperature controller of ±0.01 °C accuracy. The electrical conductivity was measured at a constant voltage (1 volt) using a programmable automatic LCR bridge (Model RM 6306 Phillips bridge).

2.3 Electrochemical measurements

For setting up the experimental cell, the pure and doped samples (active material), (80 wt%), were mixed with carbon black (10 wt%) and PVDF (10 wt%) in the presence of *n*-methylpyrrolidinone, then the mixture was left on a stirrer for 2 h to make the material homogeneous (Slurry). Then, the mixed slurry was deposited on a thin copper foil by a doctor blade process and dried at 80 °C for 2 h afterward. The covered copper foil was finally punched into round pieces with diameters of 12 mm. The as prepared electrodes were stored in a vacuum oven for further drying of another 12 h before they were transferred into a glove box for battery assembly. The glove box was circulated with argon gas (99.99%) to ensure a clear atmosphere (O_2 < 5 ppm, H_2O < 5 ppm). The counter electrode used in the half cell was lithium foil. 1 M $LiPF_6$ in ethylene carbonate (EC)–diethyl carbonate (DEC) (1 : 1 in volume) was chosen as the electrolyte. A glass fiber separator (Whatman GF/C) was used for separating the cathode and a lithium metal anode. The cells were galvanostatically charged and discharged using an Arbin battery cycler (BT2000, Arbin instruments) in the scan rate of 1 mV s^{-1} to perform charge–discharge processes for the assembled battery. The charge–discharge processes were performed at a voltage of between 0 and 3 V at different low (0.1, 0.5C) and high (2–30C) rates.

3. Results and discussions

The XRD spectra of all pure and doped samples are shown in Fig. 1A. The figure peaks showed the cubic spinel structure of the samples ($Li_4Ti_5O_{12}$) [JCPDS 26-1198] with some other intensive peaks characteristic of a crystalline second phase. The other crystalline peaks were identified as the monoclinic Li_2TiO_3 phase [JCPDS 33-0831]. The sharp crystalline peaks of both $Li_4Ti_5O_{12}$ and Li_2TiO_3 indicate a good crystalline structure with no impurity phases demonstrating that the Ni^{2+}, Cu^{2+} and Zn^{2+} ions have been successfully introduced into the lattice structure of $Li_4Ti_5O_{12}$. Another important observation from the figure is that the intensity of the Li_2TiO_3 peaks increases with the doping of Ni^{2+}, Cu^{2+} and Zn^{2+} ions. This shows that the doped samples have a high content of the crystalline second phase of Li_2TiO_3 compared to the pure one. To further confirm the doping process, quantitative X-ray analysis was performed on a definite peak of each phase. Firstly, the characteristic peak of the $Li_4Ti_5O_{12}$ phase, (111), was partially enlarged, Fig. 1B. As we can see by close inspection, there is a small shift to lower degrees for the doped samples compared to the pure one, confirming that the Ni^{2+}, Cu^{2+} and Zn^{2+} ions with a larger ionic radius (0.69 Å, 0.73 Å and 0.74 Å for Ni^{2+}, Cu^{2+} and Zn^{2+} ions, respectively) than that of Ti^{4+} (0.60 Å) have been successfully doped into the host crystal structure of $Li_4Ti_5O_{12}$. Also, the lattice parameter and unit cell volume values increase with the doped samples compared to the pure one confirming the successful doping process, as shown in Table 1. Secondly, the characteristic peak of the Li_2TiO_3 phase, (020), was also partially enlarged in Fig. 1C. The figure showed a small shift to larger degrees for the doped samples compared to the pure one, and to be more sure that this shift was caused by the crystalline second phase presence and not by the doping of any ion, the unit cell volume was calculated, as shown in Table 2, to show a stable value for all samples before and after doping. This shows that we have a good doping process into the cubic $Li_4Ti_5O_{12}$ spinel structure and not into the monoclinic Li_2TiO_3 structure. The weight ratio of Li_2TiO_3 of all the samples was estimated using the relative peak intensity, shown in Table 2. The table showed a high weight ratio of Li_2TiO_3 in all investigated samples, and a high content in the doped samples compared to the pure one.

The FT-IR spectra of the pure and doped lithium titanate composite samples calcined at 800 °C are given in Fig. 2. It can be clearly observed that there are two absorption bands located at 643 and 449 cm^{-1}. These two absorption bands indicate the symmetric and asymmetric stretching vibrations of the octahedral [TiO_6] groups respectively,[32] confirming the existence of the normal spinel structure. This is in agreement with the XRD results shown in Fig. 1. The band at 1625 cm^{-1} is attributed to the H–O–H bending vibration.[33] The band at 3470 cm^{-1} is

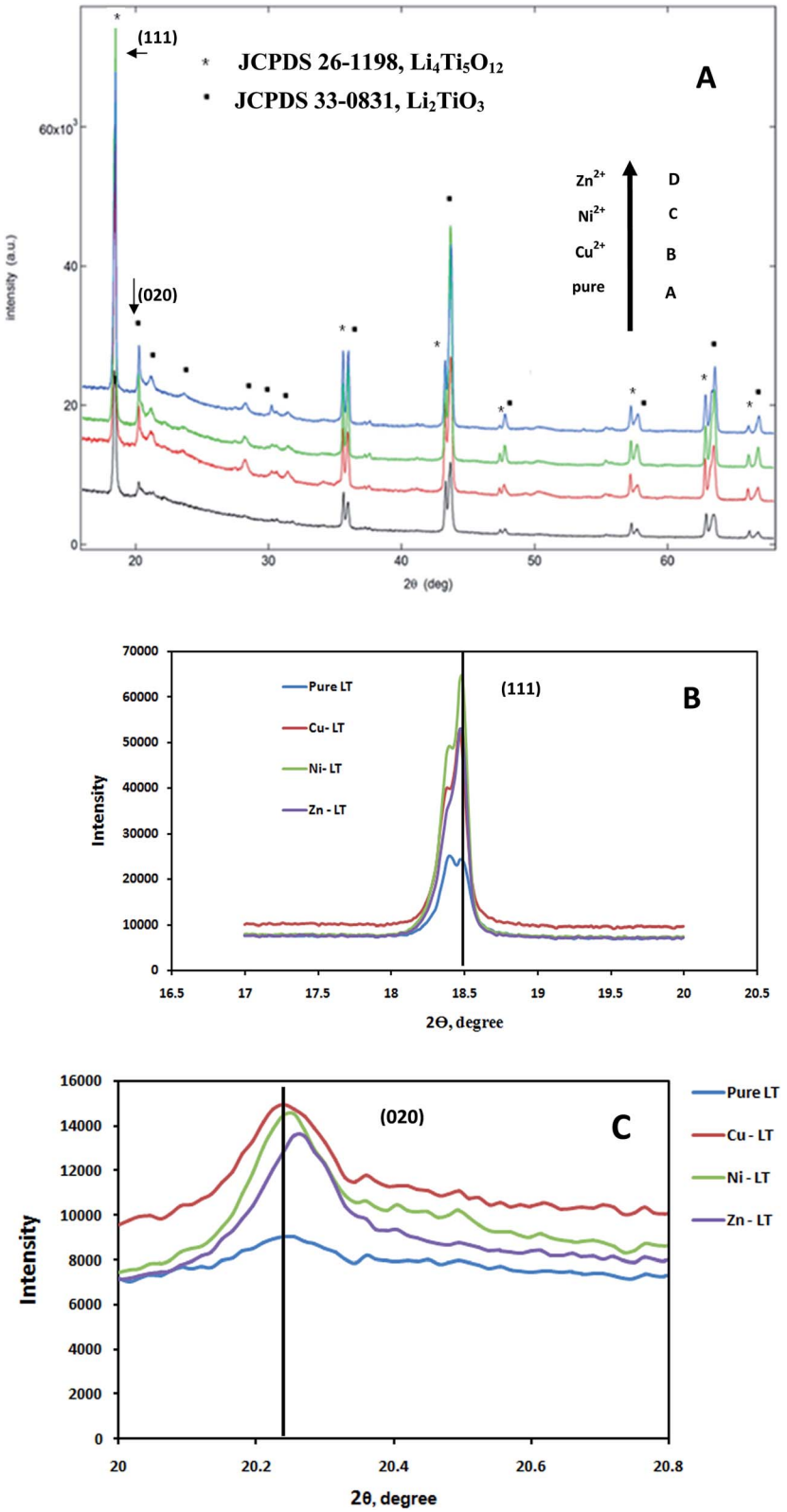

Fig. 1 X-ray diffraction patterns of (A) the pure and doped lithium titanate composites, (B) a partially enlarged drawing of the $Li_4Ti_5O_{12}$ peak (111) and (C) a partially enlarged drawing of the Li_2TiO_3 peak (020).

Table 1 Lattice parameter and unit cell volume of the $Li_4Ti_5O_{12}$ phase, calculated from X-ray peak analysis (111), in all the pure and doped lithium titanate (LT) composites

Sample	a (Å)	Unit cell volume (Å)^3
LT-pure	0.8354	583.1
LT-Ni^{2+}	0.8363	584.2
LT-Cu^{2+}	0.8368	586.1
LT-Zn^{2+}	0.8369	586.2

Table 2 Unit cell volume and weight ratio of the Li_2TiO_3 phase, calculated from X-ray peak analysis (020), in all pure and doped lithium titanate (LT) composites

Sample	Unit cell volume (Å)^3	Weight ratio (%)
LT-pure	427.01	22.23
LT-Ni^{2+}	427.01	31.50
LT-Cu^{2+}	427.01	36.77
LT-Zn^{2+}	427.01	35.60

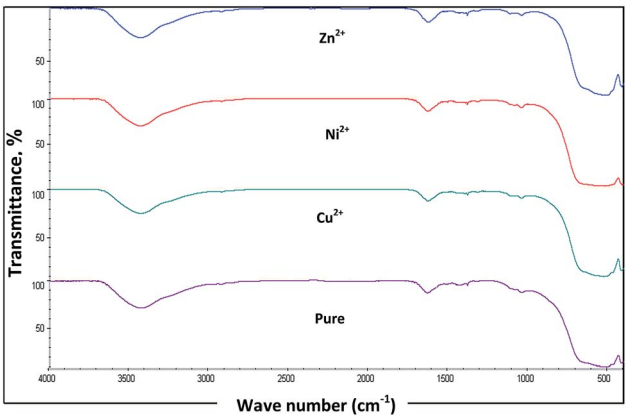

Fig. 2 FT-IR patterns of the pure and doped lithium titanate composites.

attributed to the stretching vibrations of the hydrogen-bonded OH groups.

The absence of other bands characteristic to other metal oxides also confirms the formation of the lithium titanate composites and demonstrates that all the doped ions have been introduced into the lattice structure, as confirmed by XRD.

All the SEM images of the lithium titanate composite samples calcined at 800 °C for 4 h are similar, so we took the pure lithium titanate composite sample as an example to observe the morphology of the investigated sample, as shown in Fig. 3. It can be clearly seen that the sample exhibits block-shaped particles with a varied particle size distribution. The particle size, with a wide distribution from less than 100 nm to more than 1000 nm, has a median value of approximately 500 nm.

To show the performance of the pure and doped lithium titanate composites as an anode in lithium batteries, different

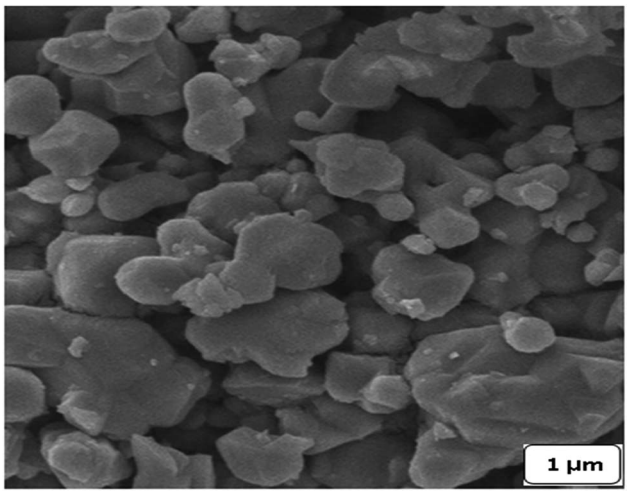

Fig. 3 SEM image of the pure lithium titanate composite.

charge–discharge processes were performed at a high rate range of 2–30C (2, 5, 10, 20, 30C) and a potential range of 0–3 V, as shown in Fig. 4.

The figure shows that all of the pure and doped lithium titanate composites have good initial discharge capacity and cycling stability throughout the high rate range (2–30C). In general, the pure lithium titanate composite showed the highest discharge capacity compared to the other ones, especially at the rates of 2 and 10C. At the same time, the Zn^{2+}-doped lithium titanate composite had the lowest discharge capacity and the Cu^{2+}-doped sample had the highest discharge capacity value compared to the Ni^{2+}-doped one only at rates of 5, 10, 20 and 30C. The only case where the Ni^{2+}-doped sample was higher than that of Cu^{2+} was observed at the rate of 2C. As the discharge rate increased, the capacities gradually decreased. More notably, at all rates of cycling performance and for all pure and doped lithium titanate composites, after the first cycle, the capacity retention begins to be more stable.

To investigate the effect of doping at low (0.1, 0.5C) and high rates (10, 20, 30C), the values of initial discharge capacity of all the investigated samples were determined, as shown in Table 3. It is obvious from the table that the Cu^{2+}-doped lithium titanate composite has the highest discharge capacity (319, 172 mA h g^{-1}) at the low rates (0.1, 0.5C), but at the high rates (10, 20, 30C), the pure sample has the highest values (123, 95, 91 mA h g^{-1}). Also, the table shows the values of lithium ion diffusion (D) calculated using the following equation,

$$D = R^2T^2/2A^2F^4\sigma^2wC^2 \quad (1)$$

where σ_w is the Warburg impedance coefficient, w, the angular frequency, R, the gas constant, T, the absolute temperature, A, the surface area, F, the Faraday's constant, and C, the molar concentration of Li ions.

The table shows that the pure lithium titanate composite has the highest lithium ion diffusion value, 5.55×10^{-13} cm^2 s^{-1}, compared to the other doped ones. At the same time, this value is higher than that of the pristine $Li_4Ti_5O_{12}$,[34] the enhancement

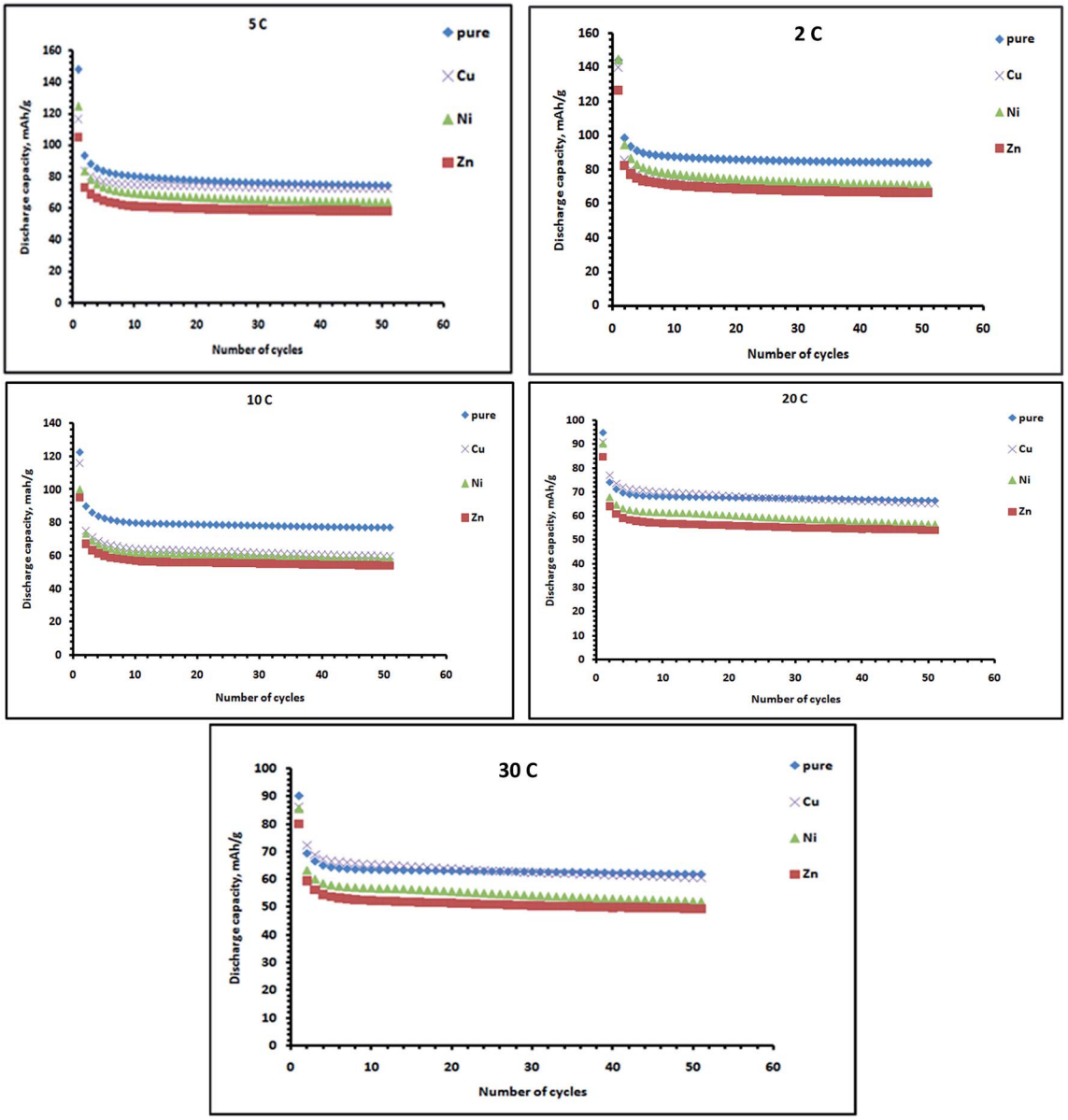

Fig. 4 Cycling performance of the pure and doped lithium titanate composites at different rates (high rate).

Table 3 Values of initial discharge capacity and Li-ion diffusion for pure and doped lithium titanate (LT) composites at low and high rates

	Initial discharge capacity (mA h g^{-1})					
Sample	0.1C	0.5C	10C	20C	30C	Li-ion diffusion, $D \times 10^{-13}$, $cm^2\ s^{-1}$
LT-pure	161	168	123	95	91	5.55
LT-Ni^{2+}	244	169	100	90	86	5.15
LT-Cu^{2+}	319	172	116	91	88	5.25
LT-Zn^{2+}	204	170	96	85	81	4.95

is caused by the low content of the Li_2TiO_3 crystalline second phase.

From all the above results, we can conclude that the lithium titanate composite samples' electrochemical performance can be divided into two parts, the pure composite is the best at the high rates (2–30C), and the Cu^{2+}-doped composite is the best at the low rates (0.1, 0.5C). This can be attributed to two different factors competing at the same time, the doping and the different content of the crystalline second phase, Li_2TiO_3. The high crystalline second phase content of the doped lithium titanate composites compared to the pure one at the high rates (2–30C) reduced the lithium ion diffusion (Table 3), and as a result, the discharge capacity reduced, showing the pure sample is the best (the crystalline content of Li_2TiO_3 is the negative predominant factor). On the other hand, at the low rates (0.1, 0.5C), the doping was the positive predominant factor, and the Cu^{2+}-doped sample is the best. The high initial discharge capacity of the Cu^{2+}-doped composite sample compared to the Ni^{2+} and Zn^{2+} ones may be attributed to the

suitable unit cell volume in the presence of the high content of Li_2TiO_3.

For the cycle life and capacity retention, all pure and doped composites showed excellent cyclability at the high rate (30C) compared to previous similar systems as will be shown hereafter, and this behavior can be attributed to structure stability against crystal breakdown due to the presence of the crystalline second phase, Li_2TiO_3. Also, presumably, the good electrochemical performance of the dual-phase $Li_4Ti_5O_{12}$–Li_2TiO_3 could be attributed to the $Li_4Ti_5O_{12}$–Li_2TiO_3 featuring abundant phase interfaces, which can possess an interfacial storage mechanism.[35–37] Namely, the lithium-ions and electrons are stored separately at the interfacial region between two neighboring phases to generate the capacitance, favoring high rate capability.[35–37]

To show the difference between the performance of the pure lithium titanate composite at low (0.1C) and high (30C) rates, the discharge capacity against cycle number (the first 10 cycles) was investigated and is shown in Fig. 5. The figure shows that the pure lithium titanate composite at the low rate delivered high initial discharge capacity, 160 mA h g^{-1}, and then a sharp decrease was observed up to 90 mA h g^{-1} to end the 10th cycle life with a capacity of 73 mA h g^{-1}. On the other hand, the pure lithium titanate composite at the high rate showed an initial discharge capacity of 91 mA h g^{-1} to end the 10th cycle with a capacity of 70 mA h g^{-1}. This shows that the pure composite at 30C has a better discharge capacity value and cycle life than that at 0.1C. Also, the coulombic efficiency was calculated for the same two samples, and is shown in Fig. 6. It is clearly shown that the 30C-pure lithium titanate composite has a higher efficiency (~100% for the last cycle) than the 0.1C one (~80% for the last cycle).

Fig. 7(A and B) show the galvanostatic lithium insertion/extraction curves for the 10th cycle of the pure lithium titanate composite at low (0.1C) and high (30C) rates between 0 and 3 V. Fig. 7B shows that the composite has two obvious almost straight regions of reduction and oxidation at about 1.5 V and 1.68 V, respectively, which are assigned to the insertion and extraction of Li^+ ions.[31] Besides the reduction–oxidation, capacitive plateaus at lower potential are also found during the scan, demonstrating that both the faradic reaction and double

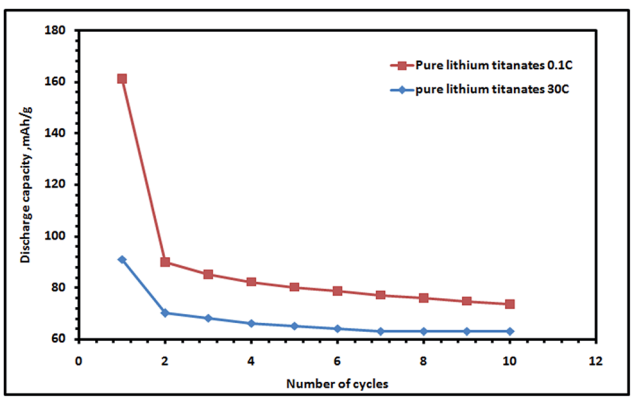

Fig. 5 Cycling performance of pure lithium titanate composite at low (0.1C) and high (30C) rates.

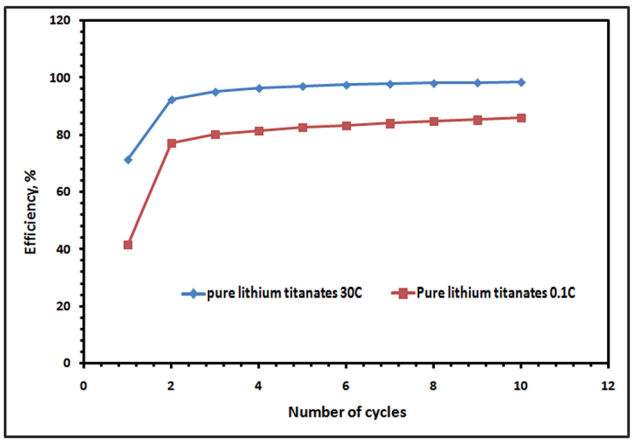

Fig. 6 Efficiency against cycle number for pure lithium titanate composite at low (0.1C) and high (30C) rates.

layer capacitance are involved in the electrochemical process.[31] In Fig. 7A, the two straight regions do not appear and the two reactions of insertion and extraction of Li^+ ions appear first as two plateaus in the ranges of 3–1 V and 1–0.5 V, respectively, and then the other two ones demonstrate both the faradic reaction and double layer capacitance like that of Fig. 7B. Here we can conclude that the pure composite at 30C has a better nature of insertion/extraction reactions than that at 0.1C.

To show the efficiency of our pure lithium titanate composite as an anode for high rate performance in lithium ion batteries, our sample was compared to the previously reported performances of pure $Li_4Ti_5O_{12}$ [34,38,39] and its composites (ref. 31) at high rates, Table 4.

To further study the properties of the pure lithium titanate composite as a good anode material for high rate performance lithium ion batteries, the AC-electrical properties (ionic conductivity and complex impedance) were also investigated at room temperature (295 K) and different frequencies, as shown in Fig. 8(A and B).

Fig. 8A shows the variation of 1og σ_{AC} against log F. It can be seen that the conductivity increases with increasing frequency. This can be attributed to the ability of the lithium cation to rotate rapidly in directions matching the direction of the applied current, demonstrating the high value of lithium ion diffusion, as shown in Table 3. Also, the ionic conductivity at $F = 1$ MHz of the pure composite was determined to equal 2.02 $\times$ 10^{-7} ohm^{-1} cm^{-1}.

The spectrum of complex impedance, Fig. 8B, shows a straight line at room temperature. This can be attributed to the blocking electrode that results in charge polarization in the bulk of the composite,[40] and as a result, the electrical double layer at each interface will lead to increased impedance against ion motion with decreasing frequency. The bulk ionic conductivity was determined to equal 2.24 $\times$ 10^{-5} ohm^{-1} cm^{-1} at $F = 1$ MHz. The equivalent circuit was also determined and is shown in Fig. 8B, where R_1 is the bulk resistance, C_1 is the bulk capacity and C_2 is the capacity of the bulk electrode–electrolyte interface. The values of dielectric constant (ε') and dielectric loss (ε'') were

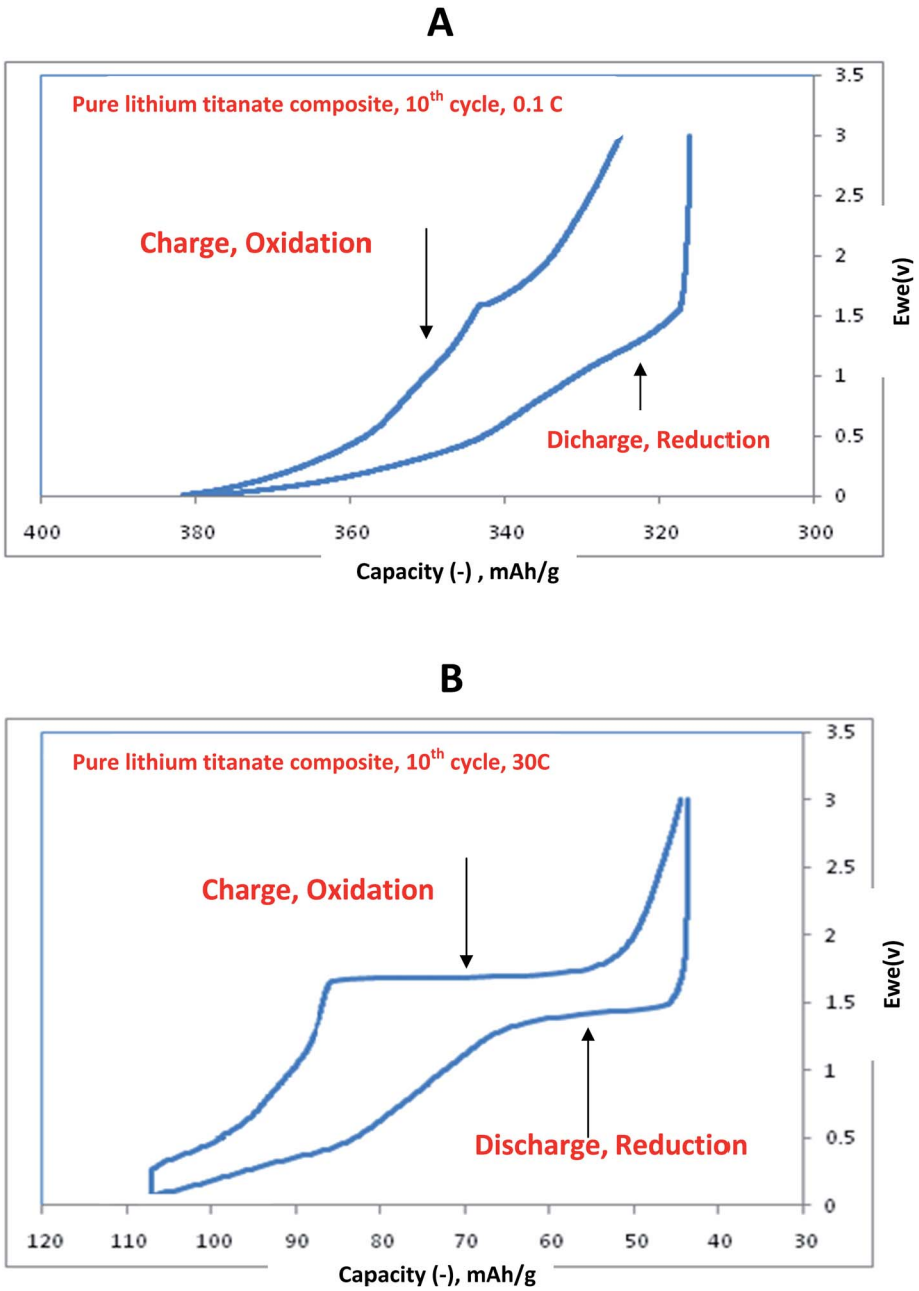

Fig. 7 Galvanostatic lithium insertion/extraction curves for the 10th cycle of the pure lithium titanate composite at low (0.1C) and high (30C) rates between 0 and 3 V.

calculated to equal 391 and 7516, respectively. All values of ionic conductivity, bulk ionic conductivity, dielectric constant and loss showed that the Li-ions have good diffusion and orientation within the crystalline network structure of the titanate composite, making it a promising anode for high rate lithium ion batteries.

Table 4 Comparison of the electrochemical properties of pure lithium titanate and its composites ($Li_4Ti_5O_{12}/Li_2TiO_3$) at high rates

Sample	Current density (C)	Potential range (V)	Initial capacity (mA h g^{-1})	Capacity retention (mA h g^{-1})	References
$Li_4Ti_5O_{12}/Li_2TiO_3$ (high content)	**30**	0–3	91	65 after 50 cycles	This work
$Li_4Ti_5O_{12}/Li_2TiO_3$ (very low content)	**10**	0–3	113	111 after 50 cycles	31
$Li_4Ti_5O_{12}$	**5**	1–2.5	33	31 after 10 cycles	34
$Li_4Ti_5O_{12}$	**30**	1–2.5	38	38 after 50 cycles	38
$Li_4Ti_5O_{12}$	**20**	0.8–2.5	62	37 after 50 cycles	39

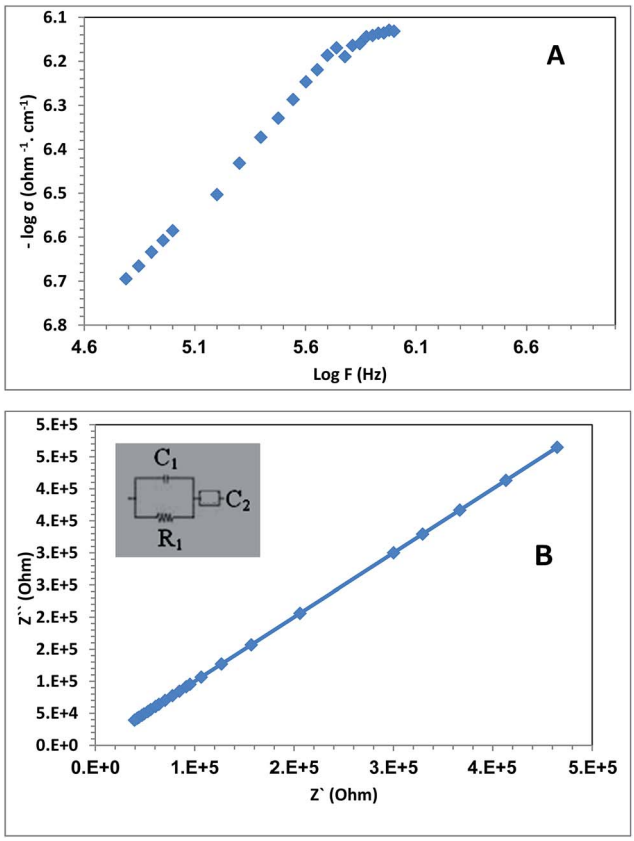

Fig. 8 AC-electrical conductivity properties; (A) frequency dependence of ionic conductivity and (B) complex impedance for the pure lithium titanate composite at room temperature (295 K).

4. Conclusions

Pure and doped lithium titanate samples containing a high crystalline second phase content of Li_2TiO_3 ($Li_4Ti_5O_{12}/Li_2TiO_3$, $Li_4Ti_{4.9}x_{0.1}O_{12}/Li_2TiO_3$, x = Ni^{2+}, Cu^{2+} and Zn^{2+}) were prepared using a simple solid state reaction. All lithium titanate composite samples were characterized using XRD, FT-IR and SEM. The XRD patterns showed a cubic spinel structure with the presence of different contents of a Li_2TiO_3 crystalline second phase. The doped samples showed a higher content of the crystalline second phase than that of the pure one. The pure lithium titanate composite showed more efficient electrochemical performance than that of the doped ones at the high discharge rates (2–30C). On the other hand, the doped lithium titanate composites showed more efficient electrochemical performance than that of the pure one at the low rates (0.1, 0.5C), and the Cu^{2+}-doped composite was the best. The efficiency and cycle stability of the pure lithium titanate composite at a high rate were higher than that at a low rate. The pure composite delivered a high initial discharge capacity of 91 mA h g^{-1} at 30C with a room temperature lithium ion diffusion of 5.55×10^{-13} cm^2 s^{-1}. After 50 cycles, the pure composite delivered a discharge capacity of 65 mA h g^{-1} at 30C, showing an excellent cycle life. The ionic conductivity, bulk ionic conductivity, dielectric constant and dielectric loss of the pure composite at room temperature and 1 MHz frequency were determined to equal 2.02×10^{-7} $ohm^{-1}cm^{-1}$, 2.24×10^{-5} ohm^{-1} cm^{-1}, 391, and 7516, respectively. The electrochemical performance of the pure composite shows a good discharge capacity with excellent cycle life at 30C, making it a promising anode material for high rate lithium-ion batteries.

Acknowledgements

I, Dr Emad M. Masoud, would like to extend my sincere thanks to Prof. Dr Juergen Meyer (Tuebingen University, Germany) for his support and helping me to perform my research activity plan through my research stay period at Germany (DAAD scholarship) (GERSS, German Egyptian Research Short-term Scholarship).

References

1 M. Armand and J. M. Tarascon, *Nature*, 2008, **451**, 652–657.
2 F. Orsini, A. Du Pasquier, B. Beaudouin, J. Tarascon, M. Trentin, N. Langenhuizen, E. de Beer and P. Notten, *J. Power Sources*, 1999, **81**, 918–921.
3 J. W. Li, A. J. Zhou, X. Q. Liu and J. Z. Li, *J. Inorg. Mater.*, 2013, **28**, 1207–1212.
4 T. Ohzuku, A. Ueda and N. Yamamoto, *J. Electrochem. Soc.*, 1995, **142**, 1431–1435.
5 K. Zaghib, M. Simoneau, M. Armand and M. Gauthier, *J. Power Sources*, 1999, **81**, 300–305.
6 A. Guerfi, S. Sevigny, M. Lagace, P. Hovington, K. Kinoshita and K. Zaghib, *J. Power Sources*, 2003, **119**, 88–94.
7 C. Chen, J. Vaughey, A. Jansen, D. Dees, A. Kahaian, T. Goacher and M. Thackeray, *J. Electrochem. Soc.*, 2001, **148**, A102–A104.
8 T. F. Yi, Y. Xie, J. Shu, Z. Wang, C. B. Yue, R. S. Zhu and H. B. Qiao, *J. Electrochem. Soc.*, 2011, **158**, A266–A274.
9 Y.-R. Jhan, C.-Y. Lin and J.-G. Duh, *Mater. Lett.*, 2011, **65**, 2502–2505.
10 Z. Wang, G. Chen, J. Xu, Z. Lv and W. Yang, *J. Phys. Chem. Solids*, 2011, **72**, 773–778.
11 T. F. Yi, J. Shu, Y. R. Zhu, X. D. Zhu, C. B. Yue, A. N. Zhou and R. S. Zhu, *Electrochim. Acta*, 2009, **54**, 7464–7470.
12 Y. H. Yin, S. Y. Li, Z. J. Fan, X. L. Ding and S. T. Yang, *Mater. Chem. Phys.*, 2011, **130**, 186–190.
13 Y. Wang, W. Zou, X. Y. Dai, L. D. Feng, H. Q. Zhang, A. J. Zhou and J. Z. Li, *Ionics*, 2014, **20**, 1377–1383.
14 T. Yuan, R. Cai and Z. Shao, *J. Phys. Chem. C*, 2011, **115**, 4943–4952.
15 L. Zhao, Y. S. Hu, H. Li, Z. Wang and L. Chen, *Adv. Mater.*, 2011, **23**, 1385–1388.
16 H. Pan, L. Zhao, Y. S. Hu, H. Li and L. Chen, *ChemSusChem*, 2011, **5**, 526–529.
17 H. Q. Zhang, Q. J. Deng, C. X. Mou, Z. L. Huang, Y. Wang, A. J. Zhou and J. Z. Li, *J. Power Sources*, 2013, **239**, 538–545, sources 239 (2013) 538e545.
18 E. Matsui, Y. Abe, M. Senna, A. Guerfi and K. Zaghib, *J. Am. Ceram. Soc.*, 2008, **91**, 1522–1527.

19 J. Lim, E. Choi, V. Mathew, D. Kim, D. Ahn, J. Gim, S. H. Kang and J. Kim, *J. Electrochem. Soc.*, 2011, **158**, A275–A280.
20 J.-G. Kim, D. Shi, M.-S. Park, G. Jeong, Y.-U. Heo, M. Seo, Y.-J. Kim, J. H. Kim and S. X. Dou, *Nano Res.*, 2013, **6**, 365–372.
21 S. Huang, Z. Wen, J. Zhang and X. Yang, *Electrochim. Acta*, 2007, **52**, 3704–3708.
22 S. Huang, Z. Wen, J. Zhang, Z. Gu and X. Xu, *Solid State Ionics*, 2006, **177**, 851–855.
23 S. Huang, Z. Wen, X. Zhu and Z. Gu, *Electrochem. Commun.*, 2004, **6**, 1093–1097.
24 C. C. Li, Q. H. Li, L. B. Chen and T. H. Wang, *ACS Appl. Mater. Interfaces*, 2012, **4**, 1233–1238.
25 M. Marinaro, F. Nobili, R. Tossici and R. Marassi, *Electrochim. Acta*, 2013, **89**, 555–560.
26 S. Huang, Z. Wen, B. Lin, J. Han and X. Xu, *J. Alloys Compd.*, 2008, **457**, 400–403.
27 J. Shu, L. Hou, R. Ma, M. Shui, L. Shao, D. Wang, Y. Ren and W. Zheng, *RSC Adv.*, 2012, **2**, 10306–10309.
28 X. Li, C. Lai, C. Xiao and X. Gao, *Electrochim. Acta*, 2011, **56**, 9152–9158.
29 M. M. Rahman, J. Z. Wang, M. F. Hassan, D. Wexler and H. K. Liu, *Adv. Energy Mater.*, 2011, **1**, 212–220.
30 Y. Q. Wang, L. Gu, Y. G. Guo, H. Li, X. He, S. Tsukimoto, Y. Ikuhara and L. Wan, *J. Am. Chem. Soc.*, 2012, **134**, 7874–7879.
31 Y. Wang, A. Zhou, X. Dai, L. Feng, J. Li and J. Li, *J. Power Sources*, 2014, **266**, 114–120.
32 P. P. Prosini, R. Mancini, L. Petrucci, V. Contini and P. Villano, *Solid State Ionics*, 2001, **144**(1), 185.
33 S. Y. Venyaminov and F. G. Prendergast, *Anal. Biochem.*, 1997, **248**, 234–245.
34 C. Lin, M. O. Lai, L. Lu, H. Zhou and Y. Xin, *J. Power Sources*, 2013, **244**, 272–279.
35 M. M. Rahman, J. Z. Wang, M. F. Hassan, S. Chou, D. Wexler and H. K. Liu, *J. Power Sources*, 2010, **195**, 4297.
36 J. Jamnik and J. Maier, *Phys. Chem. Chem. Phys.*, 2003, **5**, 5215.
37 X. Q. Yu, J. P. Sun, K. Tang, H. Li, X. J. Huang, L. Dupont and J. Maier, *Phys. Chem. Chem. Phys.*, 2009, **11**, 9497.
38 C.-Y. Lin and J. G. Duh, *J. Alloys Compd.*, 2011, **509**, 3682–3685.
39 G.-Y. Liu, H.-Y. Wang, G.-Q. Liu, Z.-Z. Yang, B. Jin and Q.-C. Jiang, *Electrochim. Acta*, 2013, **87**, 218–223.
40 E. M. Masoud, *J. Alloys Compd.*, 2015, **651**, 157–163.